

Hysteresis-Free Contact Doping for High-Performance Two-Dimensional Electronics

Po-Hsun Ho,^{*,○} Jun-Ru Chang,[○] Chun-Hsiang Chen, Cheng-Hung Hou, Chun-Hao Chiang, Min-Chuan Shih, Hung-Chang Hsu, Wen-Hao Chang, Jing-Jong Shyue, Ya-Ping Chiu,^{*} and Chun-Wei Chen^{*}



Cite This: *ACS Nano* 2023, 17, 2653–2660



Read Online

ACCESS |

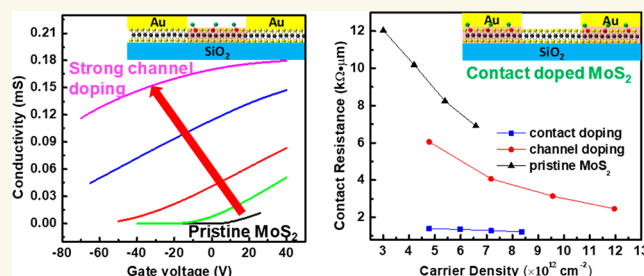
Metrics & More

Article Recommendations

Supporting Information

ABSTRACT: Contact doping is considered crucial for reducing the contact resistance of two-dimensional (2D) transistors. However, a process for achieving robust contact doping for 2D electronics is lacking. Here, we developed a two-step doping method for effectively doping 2D materials through a defect-repairing process. The method achieves strong and hysteresis-free doping and is suitable for use with the most widely used transition-metal dichalcogenides. Through our method, we achieved a record-high sheet conductance ($0.16 \text{ mS}\cdot\text{sq}^{-1}$ without gating) of monolayer MoS_2 and a high mobility and carrier concentration ($4.1 \times 10^{13} \text{ cm}^{-2}$). We employed our robust method for the successful contact doping of a monolayer MoS_2 Au-contact device, obtaining a contact resistance as low as $1.2 \text{ k}\Omega\cdot\mu\text{m}$. Our method represents an effective means of fabricating high-performance 2D transistors.

KEYWORDS: two-dimensional materials, contact doping, *n*-type doping, hysteresis, transistors, contact resistance, scanning tunneling microscopy



Two-dimensional (2D) materials are expected to exhibit favorable immunity to the short-channel effect because of their atom-thick layer structure and lack of surface dangling bonds.¹ However, the considerable metal–2D material contact resistance is the key issue to be overcome for the realization of practical applications.^{2–5} The contact resistance is due to the strong Fermi level pinning between the metal and 2D materials causing a large Schottky barrier height and width,^{6–8} which results in considerable contact resistance. The most effective method of reducing the Schottky resistance is contact doping.⁹ As with silicon, ion implantation has been widely used to reduce contact resistance.¹⁰ However, this approach cannot be used for monolayer 2D materials because the energetic ions damage the fragile materials.^{11–13} Substitutional doping^{14,15} can only be achieved at high temperatures through conventional chemical vapor deposition (CVD), which limits this kind of doping to the contact region. Many studies have transferred the heavily doped 2D layer onto the undoped 2D layer to reduce the contact resistance and control the carrier type.^{16,17} However, processes requiring multiple transfers are impractical, and the van der Waals gap between two 2D layers limits the ultimate contact resistance.¹⁸ As for surface charge transfer doping with doping molecules^{19–23} or layers,^{24–28} the nonconductive dopant in the contact region blocks the transport path and causes the degradation of the

device performance. In addition to reducing the contact resistance, the large hysteresis and instability of the doping process is another crucial issue to be tackled.^{19–22} Another promising doping method is covalently functionalized doping, which is achieved through a chemical reaction between the doping molecules and 2D materials.^{29–32} The bonded molecules donate charge to the underlying 2D materials. Because of the formation of strong covalent bonds between dopants and 2D materials, this method could achieve high stability. However, the drawback of this method is that it still slightly alters the structure, potentially resulting in mobility degradation.³² In this study, we developed a robust, covalently functionalized doping method by a defect-repairing process, which is called two-step doping. The intermediate products of the reaction between a base and a carbonyl group can bond to the chalcogenide vacancies of 2D materials, resulting in *n*-type doping. The doping concentration can be controlled by

Received: October 25, 2022

Accepted: January 26, 2023

Published: January 30, 2023



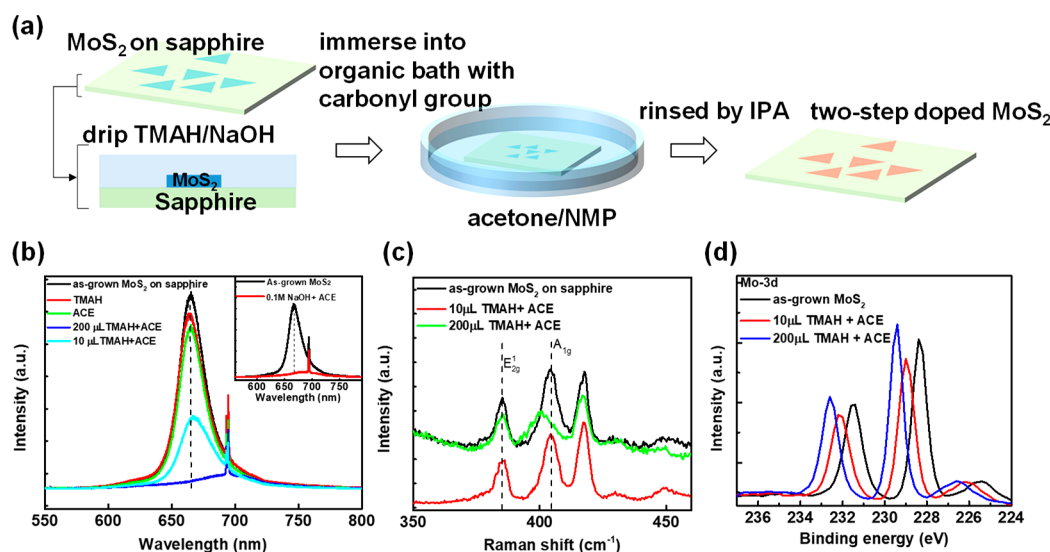


Figure 1. Process and optical characterizations of two-step *n*-type doping. (a) Process flow for two-step doping. (b) Photoluminescence spectra of the pristine CVD, acetone, TMAH, and two-step treated MoS₂. The inset is the spectra of two-step-doped MoS₂ with 0.1 M NaOH and acetone (ACE). (c) Raman spectra of the MoS₂ with different doping recipes. (d) XPS data of Mo 3d spectra of pristine, lightly (10 μ L) two-step-doped, and heavily (200 μ L) two-step-doped MoS₂.

controlling the amount of base and can reach $4.1 \times 10^{13} \text{ cm}^{-2}$ on MoS₂. The MoS₂ doped through our two-step process can maintain a high mobility even when heavily doped, resulting in a record-high sheet conductivity ($0.16 \text{ mS}\cdot\text{sq}^{-1}$) without gating. The defect-repairing doping process can be applied to the most widely used transition-metal dichalcogenide (TMD) monolayers. Moreover, we discovered that devices fabricated with this method exhibited no hysteresis or doping degradation even after 250 °C annealing because of the formation of chemical bonds. The contact-doped device based on the two-step doping process demonstrated the lowest contact resistance reported to date for an Au-contact monolayer MoS₂ system. This hysteresis-free contact doping indicates that our two-step doping method is promising for the development of high-performance 2D electronics.

RESULTS AND DISCUSSION

Our proposed two-step doping was performed during the hydrolysis of the carbonyl group in a basic environment.³³ To implement and test our method, first we dripped a small amount (200 μ L) of a 2.38% tetramethylammonium hydroxide (TMAH, an organic base) solution onto as-grown MoS₂ on sapphire through CVD, as illustrated in Figure 1a. Subsequently, 10 mL of acetone was poured on the MoS₂ to drive the doping reaction. The base concentration should be low enough to avoid the formation of residues due to the ketone condensation process,³⁴ as shown in Figure S1. We confirmed the doping effect through photoluminescence measurements, as illustrated in Figure 1b. The photoluminescence of MoS₂ was largely quenched and shifted to a lower energy, which indicates the common phenomenon of trion formation under a high carrier concentration.^{26,35} To make a control sample, we also dripped pure acetone and pure TMAH on two other MoS₂ samples and measured their photoluminescence. We observed no obvious photoluminescence change in these samples, indicating that neither the acetone nor TMAH had a doping effect on the MoS₂. We also found that the *n*-doping effect was much weaker if we mixed TMAH and acetone first instead of using the two-step process (Figure S2). This is because TMAH

adsorbed on the 2D material first and then formed the intermediate at the 2D surface in the two-step doping process instead of dispersing in the whole solution. In addition, we performed the two-step doping process with 0.1 M NaOH (inorganic base) and acetone. The photoluminescence quenching was similar to that of the acetone–TMAH system, as shown in the inset of Figure 1b, indicating that this effect results from the intermediate product of the reaction of the base and acetone. However, an alkali base is usually avoided in the device fabrication process because of its potential to damage the gate dielectric. We used TMAH as the base for the other experiments in this work. We also used another organic molecule, *N*-methyl-2-pyrrolidone (NMP), with a carbonyl group to replace acetone and obtained a similar doping result, as shown in Figure S3. These experiments confirm that the doping effect is from the reaction between the carbonyl group and the base. The doping concentration could also be controlled by the base amount, where the PL intensities are gradually quenched from the pristine sample to the doped samples with 10 and 200 μ L of TMAH, as seen in Figure 1b. Raman spectra (Figure 1c) revealed only an evident redshift of the A_{1g} peak, which had a much lower intensity than that of the pristine case, a result in agreement with the previously reported *n*-type doping phenomenon. The strong coupling of electrons and phonons was assumed to be responsible for the redshift of the A_{1g} peak.³⁶ By contrast, we observed no clear shift in the in-plane E_{2g} peak after doping, indicating that no structural damage or additional strain occurred during the two-step doping process. We also evaluated the two-step doping through X-ray photoluminescence spectroscopy (XPS). Figure 1d presents the binding energy of the Mo 3d orbital. As the doping concentration increased, the binding energy gradually shifted to a higher-energy region, indicating a larger difference between the Fermi level and core-level energies.^{19,25} This tunable binding energy shift confirms the controllability of the two-step doping.^{19,25,36}

From our results, we inferred that the doping occurred when the MoS₂ had contact with the intermediate product of the base and the carbonyl compound. Generally, the hydrolysis

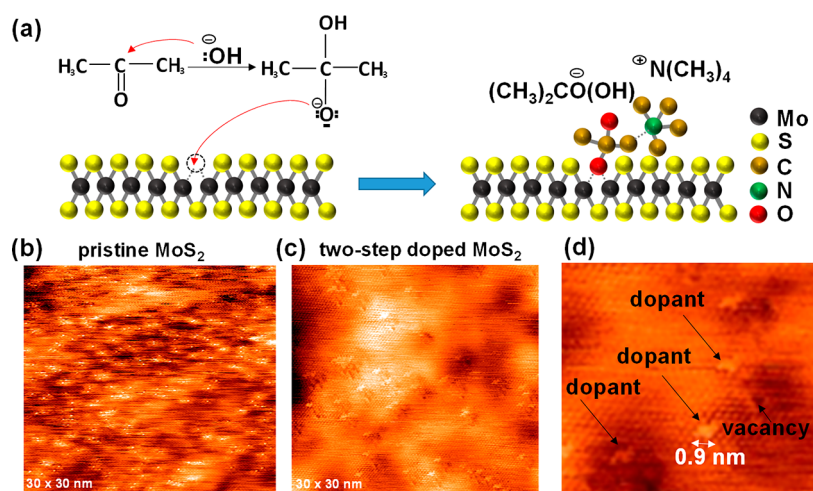


Figure 2. Doping mechanism and STM analyses of two-step doping. (a) Mechanism of two-step doping in the MoS_2 system. (b) STM tomography image (positive bias) of pristine MoS_2 on the SiO_2 substrate. Small white spots are the sulfur vacancy sites. (c) STM image (negative bias) of the two-step-doped MoS_2 . (d) Zoomed-in image (negative bias) of the two-step-doped MoS_2 . The black spots are sulfur vacancies, and the white double-cross shapes are the regions with dopants on top of the MoS_2 .

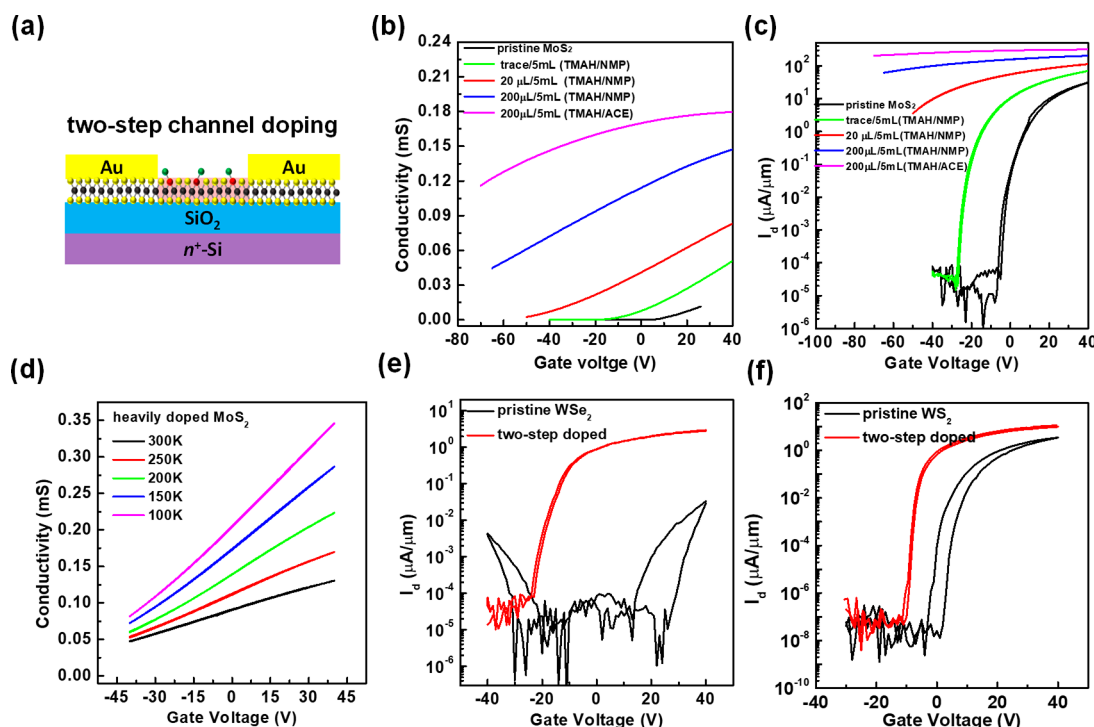


Figure 3. Electrical characteristics of the channel-doped 2D transistors. (a) Schematic image of a FET with two-step-doped MoS_2 . (b) Gate-dependent conductivity of the MoS_2 FETs with different doping recipes. (c) Log plot of device performance with different doping recipes. (d) Gate-dependent conductivity of a heavily doped MoS_2 FET at different temperatures. (e and f) Output characteristic of the WSe_2 and WS_2 FETs, respectively, with and without two-step doping.

reaction between a carbonyl group and a base forms a nucleophilic functional group $(\text{CH}_3\text{COCH}_3\text{OH})^-$ that attacks sites with partial positive charge or defects. Inherent sulfur vacancies are common in MoS_2 .^{37–39} These vacancies tend to be attacked by the nucleophilic agent, as illustrated in Figure 2a. After the reaction, the remaining positive ions $\text{N}(\text{CH}_3)_4^+$ settle near the dopants and maintain the charge neutrality of the system. The lack of a steric effect also enhances the reaction between the nucleophile and MoS_2 in the 2D system. This proposed mechanism was further confirmed through scanning tunneling microscopy (STM). Figure 2b presents a

STM tomography image of pristine MoS_2 . The constant-current image (positive bias) reveals a high density of sulfur vacancies ($2.2 \times 10^{13} \text{ cm}^{-2}$) in the monolayer MoS_2 , which is consistent with the sulfur vacancy density in the previous works.^{37,39} After two-step doping (Figure 2c and d), we observed numerous double-cross-shaped features under a negative bias, which are evidence of the dopants on the MoS_2 surface. The double-cross shapes appeared to be approximately 0.9 nm across, approximately the size of the intermediate product of the reaction of TMAH and acetone (Figure 2a). The sulfur vacancies under a negative bias appear

as black dots, as shown in Figure 2d. As seen from Figure 2b and d, the density of sulfur vacancies obviously decreases after two-step doping, which supports our proposed mechanism in which the two-step dopants tend to bond to the vacancy sites. The bonding between the dopants are also evident in the XPS spectra shown in Figure S4. The formation of the C–O–Mo bond contributes to the oxygen peak at 531.4 eV. The combination of the real-space STM image and the XPS chemical bonding information provides evidence that dopants are bonded to the defect sites.

Next, we analyzed the *n*-doping properties by fabricating field-effect transistors (FETs), as shown in Figure 3a. We employed a back-gate device with Au contacts for the source and drain electrodes. The pristine MoS₂ device exhibited a standard *n*-type behavior when the threshold voltage (V_T) was set to 11 V. We doped MoS₂ devices with different concentrations of TMAH in NMP or acetone. The device revealed a controllable negative shift in the threshold voltage, as illustrated in Figures 3b and S5 (in the Supporting Information). Because our MoS₂ was grown by the CVD method, there was some variation in the defect density at each round. The highest doping concentration calculated from the threshold voltage shift was $4.1 \times 10^{13} \text{ cm}^{-2}$, which was stronger than the reported *n*-doping of MoS₂ systems achieved in previous studies.^{19,20,24,26,27} Notably, the hysteresis (Figure 3c) of the device was significantly suppressed after two-step doping because the dopants could directly bond to the original defect sites (sulfur vacancies). This defect-repairing doping process not only reduces the hysteresis but also preserves the channel mobility. Figure S5 presents a plot of the channel mobility versus the doping concentration. The devices exhibit high mobilities at a high carrier density range of around $0.5\text{--}3 \times 10^{13} \text{ cm}^{-2}$ because of the Schottky barrier thinning effect due to doping. The result indicates that the defect-repairing doping mechanism does not cause strong scattering from charge impurities. The high doping concentration and high mobility contribute to such a high sheet conductivity ($\sigma = nq\mu = 0.16 \text{ mS}\cdot\text{sq}^{-1}$) at $V_{\text{BG}} = 0 \text{ V}$, which is currently the highest reported value for monolayer MoS₂ without gating. Figure 3d illustrates the temperature-dependent characteristics of a heavily doped ($n = 2 \times 10^{13} \text{ cm}^{-2}$) MoS₂ device. We observed a significant mobility enhancement of the device at low temperatures. This effect indicates two key facts: (1) Phonon scattering still dominated the transport behavior instead of charge impurities,⁴⁰ even with such a high doping concentration. (2) The Schottky barrier width greatly decreased after doping, so no large increase in the Schottky resistance occurred, even at low temperatures. Because two-step doping relies on the chalcogenide defects of TMDs, we expected this method was applicable to other widely used monolayers TMDs, such as WSe₂ and WS₂, and therefore tested these materials. Figure 3e and f present the transport properties of WSe₂ and WS₂ after two-step doping. Both systems exhibited clear *n*-type doping without hysteresis, confirming that defect repair occurs during our two-step doping process.

Another key property of our two-step doping process is its stability. To test the stability, we performed vacuum annealing at 250 °C on the two-step-doped MoS₂ device and then obtained electrical measurements at room temperature, as illustrated in Figure 4a. The on-current and mobility of the devices barely changed after annealing, demonstrating the robustness of the doping achieved through this method. The favorable thermal stability resulted from the covalent bonding

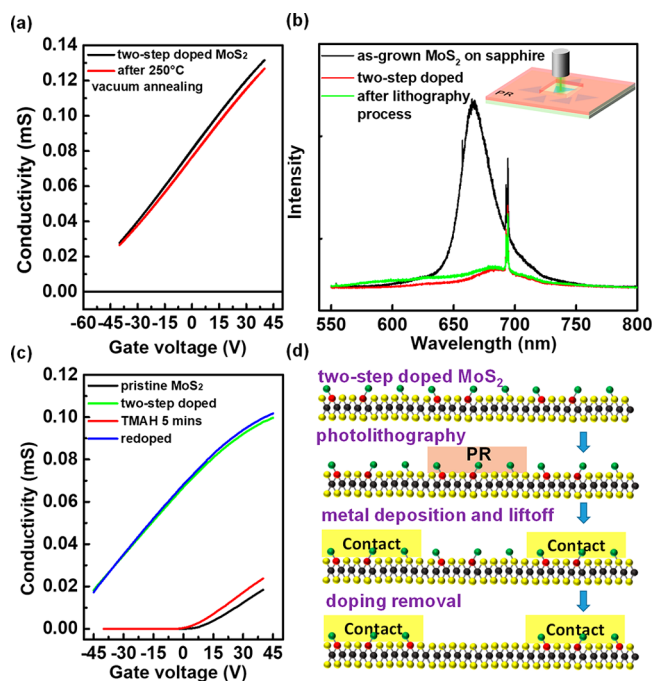


Figure 4. Stability of two-step doping and the contact doping approach. (a) Gate-dependent conductivity of the two-step-doped MoS₂ device before and after 250 °C annealing. (b) Photoluminescence spectra of the two-step-doped MoS₂ before and after the photolithography process. (c) Reversible doping effect of a two-step-doped MoS₂ device. (d) Schematic images of the contact doping process.

between the dopants and MoS₂. Such stability is essential for subsequent processes, such as atomic layer deposition or plasma-enhanced CVD, which are widely used for the fabrication of the dielectric layer. In addition, chemical resistance to lithography is important for device integration. We conducted traditional photolithography on the two-step-doped MoS₂ and used photoluminescent spectroscopy to confirm that it remained doped afterward. The photoluminescence spectra in Figure 4b indicate that trions still dominated the emission of the two-step-doped MoS₂ after the lithography process. Thus, doping through our two-step method is robust to the photolithography process, enabling its use in contact doping. Although the two-step doping is robust and stable, it can still be chemically reversed. Two-step doping through our method can be chemically removed through a period of immersion in high-concentration TMAH. The high concentration of OH[−] groups wrests the molecular N(CH₃)₄⁺ that balances the charge neutrality in the beginning condition, which makes (CH₃COCH₃OH)[−] unstable on the MoS₂. The (CH₃COCH₃OH)[−] thus gradually detaches from the MoS₂ surface, resulting in the removal of doping. Figure 4c illustrates the device characteristics after such a chemical treatment. The current and threshold voltage shifted back to those of pristine MoS₂, indicating the successful chemical removal of the doping. We subsequently redoped the channel through the two-step process. The output current and V_T shifted back to the values of the device after the first round of doping. With this kind of doping flexibility, we developed the contact doping process illustrated in Figure 4d. We first doped the entire monolayer MoS₂ film and then formed the source and drain electrodes through photolithography. Next, the channel doping was removed through immersing the film in

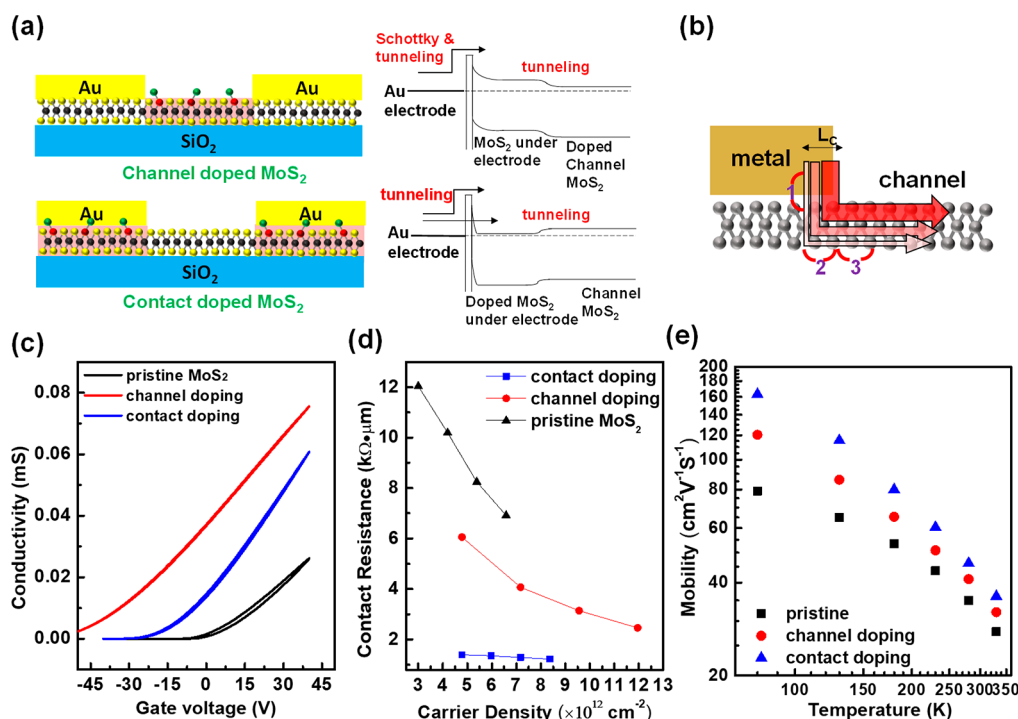


Figure 5. Comparison of the pristine, channel-doped, and contact-doped MoS₂ devices. (a) Schematic images of the channel-doped (top) and contact-doped (bottom) MoS₂ devices. The right band diagrams correspond to the left device structures. (b) Schematic image of the current flow in the contact regions. (c) Gate-dependent characteristic of pristine, channel-doped, and contact-doped MoS₂. (d) Contact resistances of devices with different doping methods. (e) Temperature-dependent mobilities of devices with different doping methods.

20% TMAH for 5 min. Unlike previous studies that usually doped the entire channel, we can maintain the intrinsic channel to ensure the good on–off behavior of the transistors. It is worth noting that the removal of doping can be only carried out with the chemical reaction by using a strong and high-concentration base. Without such chemical treatment, the dopants exhibit excellent stability by forming covalent bonding with the vacancy sites on the MoS₂ surface.

Next, we would like to compare the device performance with contact doping to that with conventional channel doping. Figure 5a shows schematic illustrations of the device structures and the corresponding band diagrams with channel doping and contact doping. Generally, the contact resistance comprises three components (Figure 5b).⁴¹ The first component (1) is the vertical Schottky and tunneling resistance between the metal and the 2D material under the metal. This resistance was expected to be strongly reliant on the doping level of the 2D region under the metal. The second component (2) is the lateral resistance along the transfer length (L_c) region under the contacts. This resistance was expected to strongly depend on the sheet conductivity of the 2D material under the metal. The final component (3) is the lateral Schottky resistance between the 2D channel and the 2D material under the metal. Typically, channel doping only reduces the Schottky barrier height between the 2D channel and the 2D region under the metal (corresponding to component (3).) Channel doping usually improves the contact resistance but also causes a low on–off ratio (as shown in Figure 3c). Moreover, the (1) and (2) components are not improved because the 2D material under the metal remains undoped, as shown in Figure 5b. It has been shown that gating the 2D region under metals is difficult with a back-gate device because of strong Fermi level pinning,⁴² which limits the device performance. By contrast,

contact doping is crucial for reducing both the vertical and lateral Schottky resistance by heavily doping the 2D region under the metal. As displayed in the bottom right of Figure 5a, both the vertical (component (1)) and lateral (component (3)) Schottky resistances can be greatly reduced by contact doping through our two-step doping process. Tunneling became the main transport behavior at both junctions. In addition, the highly conductive 2D region under the metal also improved the lateral transport within the transfer length region (the (2) component). Figure 5c illustrates the output characteristics of devices doped through different doping methods. The contact-doped device exhibited higher two-probe mobility than the pristine or channel-doped MoS₂ device. Furthermore, the on–off ratio of the device with contact doping remained higher ($\sim 10^8$; Figure S6) than that of the channel-doped device due to its intrinsic channel. As mentioned above, the higher device mobility was due to the lower contact resistance. We determined the contact resistances of the pristine, channel-doped, and contact-doped MoS₂ devices using the transfer length method (Figures 5d and S7). At the same carrier concentration ($n = 6.5 \times 10^{12} \text{ cm}^{-2}$), the contact resistance of the channel-doped device ($4.5 \text{ k}\Omega\cdot\mu\text{m}$) was $0.65\times$ that of the pristine MoS₂ device ($6.9 \text{ k}\Omega\cdot\mu\text{m}$). The contact resistance of the contact-doped device was improved to be $1.2 \text{ k}\Omega\cdot\mu\text{m}$, which is $0.18\times$ that of the pristine MoS₂ device, exhibiting the lowest contact resistance reported for an Au-contact monolayer MoS₂ system. This substantial improvement was due to the lower Schottky resistance at both the vertical and lateral junctions. The reduced Schottky resistance effect was also supported by temperature-dependent measurements (Figure S8). Generally, the Schottky resistance is higher at low temperatures because thermionic emission relies strongly on the temperature. This

limits the improved mobility at low temperatures because of the limited phonon scattering.^{40,43} Figure 5e illustrates the temperature-dependent mobility of each device. The contact-doped device exhibited a greater mobility enhancement than the channel-doped or pristine MoS₂ device at a low temperature. The results indicate that the Schottky resistance of the contact-doped device was reduced.

CONCLUSIONS

In conclusion, we developed a two-step doping process (also called the defect-repairing doping process) to enable hysteresis-free and robust doping without adversely affecting the mobility of 2D materials. We achieved ultrastrong doping of MoS₂ with a carrier concentration reaching $4.1 \times 10^{13} \text{ cm}^{-2}$ and a record-high sheet conductivity ($0.16 \text{ mS}\cdot\text{sq}^{-1}$) without additional gating. With such a stable and strong doping, a contact-doped MoS₂ device was fabricated with the lowest contact resistance ($1.2 \text{ k}\Omega\cdot\mu\text{m}$). The method can also be applied to the most widely used TMDs with chalcogenide defects. Our two-step doping process enables stable doping for applications in high-performance 2D electronics.

METHODS

MoS₂ Growth. The MoS₂ used in the work was prepared by the self-capping vapor–liquid–solid method.⁴⁴ In brief, the NaF/SiO₂/MoO₃/sapphire stack was first prepared by thermal evaporation (2 nm MoO₃ and 20 nm NaF) and sputtering (7 nm SiO₂) powders onto a sapphire substrate. The sample and sulfur powder were placed in the quartz boats and then placed in the three-zone furnace. The temperature at the sample (third zone) ramped up at a rate of $40 \text{ }^\circ\text{C}\cdot\text{min}^{-1}$ to $800 \text{ }^\circ\text{C}$ and was held for 10 min. Sulfur vapor was introduced by ramping up the temperature at the first zone at a rate of $15 \text{ }^\circ\text{C}\cdot\text{min}^{-1}$, and the temperature was held at $140 \text{ }^\circ\text{C}$ during growth. The growth pressure was kept at 30 Torr. After growth, the furnace was shut down and fast-cooled using an industrial fan.

WS₂ and WSe₂ Growth. WS₂ was grown by the traditional CVD method. 0.3 g of WO₃ and 0.8 g of sulfur powders were placed in quartz boats. The WO₃ boat was placed in the center of the furnace, and the sulfur boat was put outside of the heating zone and heated by the band heater. The furnace was heated to $920 \text{ }^\circ\text{C}$ with a $30 \text{ }^\circ\text{C}\cdot\text{min}^{-1}$ ramp rate for a 10 min growth. The band heater was kept at $160 \text{ }^\circ\text{C}$ during growth. During the growth process, the flow rate of Ar/H₂ was tuned and optimized at 200:10 sccm and the growth pressure was 15 Torr. After the reaction, the furnace was naturally cooled to room temperature under 200:10 sccm Ar/H₂. For the WSe₂ growth, it was similar to the WS₂ system except that 0.8 g of selenium powder was used instead of sulfur. The furnace was heated to $950 \text{ }^\circ\text{C}$ and held at that temperature for a 10 min growth. The temperature of the selenium was kept at $300 \text{ }^\circ\text{C}$ during the growth, and the total pressure of the system was set at 1 Torr.

Two-Step Doping. As-grown or transferred TMDs were first placed in the beaker. A suitable amount (20–200 μL) of base (2.38% TMAH or 0.1 M NaOH) was dripped on the TMDs and held for 3 min. Then, 10 mL of acetone or *N*-methyl-2-pyrrolidone (NMP) was poured into the beaker to trigger the reaction. After 30 min, TMD samples were rinsed in isopropanol three times to fully clean the doping residue.

Device Fabrication and Characterization. Monolayer TMD was transferred by the poly(methyl methacrylate) (PMMA) method. A thin PMMA layer was spin-coated on the as-grown TMD film on sapphire. Water or NaOH was used to detach the PMMA/TMD stack and the sapphire substrate. The PMMA/TMD stack was picked up by a heavily *p*-doped silicon substrate with 90 nm thermal oxide. The PMMA was dissolved in acetone, leaving monolayer TMD on the substrates. Optical lithography and oxygen plasma were used to define the MoS₂ strips. Then, the second lithography process defined the source-drain patterns. A 50 nm gold layer was thermally evaporated

under a high vacuum as the source-drain and back-gate electrodes. For the contact doping device, the as-defined MoS₂ strips were first two-step-doped before the source-drain lithography. After the source-drain liftoff, the devices were immersed in 5% TMAH for 5 min to erase the doping in the channel region. Before the electrical properties were measured, the FETs were annealed at $120 \text{ }^\circ\text{C}$ under a 10^{-3} Torr vacuum for 10 h in a probe station (Lakeshore). Gate and source-drain voltages were applied by Keithley 6487 picometers. Raman and photoluminescence spectra were measured by a confocal system equipped with a 532 nm laser. XPS spectra were obtained using the PHI VersaProbe system.

STM Measurements. Both the pristine and two-step-doped MoS₂ FET devices on a 90 nm SiO₂/Si substrate were directly used as the samples for the STM measurement. STM experiments were performed in an ultrahigh vacuum (UHV) under a background pressure of less than 1×10^{-10} Torr. STM and spectroscopy images were simultaneously acquired at a temperature of 300 K. Topographic imaging was conducted at a constant current of 0.1 nA and at the +0.5 and −0.5 V sample voltages.

ASSOCIATED CONTENT

Supporting Information

The Supporting Information is available free of charge at <https://pubs.acs.org/doi/10.1021/acsnano.2c10631>.

Additional doping result of a high-concentration base, photoluminescence spectra, doping result of NMP-TMAH, XPS spectra, doping concentration extraction, log plots of devices, TLM method, and temperature-dependent characteristics of devices (PDF)

AUTHOR INFORMATION

Corresponding Authors

Po-Hsun Ho – Department of Materials Science and Engineering, National Taiwan University, Taipei 106, Taiwan; Center of Atomic Initiative for New Materials, National Taiwan University, Taipei 106, Taiwan; orcid.org/0000-0001-8319-0556; Email: river770323@gmail.com

Ya-Ping Chiu – Department of Physics and Center of Atomic Initiative for New Materials, National Taiwan University, Taipei 106, Taiwan; Email: ypchiu@phys.ntu.edu.tw

Chun-Wei Chen – Department of Materials Science and Engineering, National Taiwan University, Taipei 106, Taiwan; Center of Atomic Initiative for New Materials, National Taiwan University, Taipei 106, Taiwan; orcid.org/0000-0003-3096-249X; Email: chunwei@ntu.edu.tw

Authors

Jun-Ru Chang – Department of Materials Science and Engineering, National Taiwan University, Taipei 106, Taiwan

Chun-Hsiang Chen – Department of Physics, National Taiwan University, Taipei 106, Taiwan

Cheng-Hung Hou – Research Center for Applied Sciences, Academia Sinica, Taipei 11529, Taiwan

Chun-Hao Chiang – Department of Materials Science and Engineering, National Taiwan University, Taipei 106, Taiwan; orcid.org/0000-0002-9066-4657

Min-Chuan Shih – Department of Physics, National Taiwan University, Taipei 106, Taiwan

Hung-Chang Hsu – Department of Physics, National Taiwan University, Taipei 106, Taiwan

Wen-Hao Chang – Department of Electrophysics, National Yang Ming Chiao Tung University, Hsinchu 300, Taiwan; orcid.org/0000-0003-4880-6006

Jing-Jong Shyue – Research Center for Applied Sciences, Academia Sinica, Taipei 11529, Taiwan; orcid.org/0000-0002-8508-659X

Complete contact information is available at:
<https://pubs.acs.org/10.1021/acsnano.2c10631>

Author Contributions

○P.-H.H. and C.-R.C. contributed equally to this work.

Notes

The authors declare no competing financial interest.

ACKNOWLEDGMENTS

C.W.C. would like to thank the Minister of Science and Technology (MOST), Taiwan, and the Taiwan Consortium of Emergent Crystalline Materials (TCECM) (project nos. 107-2119-M-002-028-MY2, 107-2112-M-002-024 -MY3, 107-2112-M-009-024-MY3, and 108-2119-M-009-011-MY3) for financial support. Financial support by the Center of Atomic Initiative for New Materials (AI-Mat), National Taiwan University, from the Featured Areas Research Center Program within the framework of the Higher Education Sprout Project by the Ministry of Education in Taiwan (Grant 108L9008) is also acknowledged. Y.P.C. would like to thank MOST of Taiwan (contract nos. MOST 109-2628-M-002-005-MY3 and MOST 110-2622-8-002-014) and National Taiwan University (contract nos. NTU-110L7839 and NTU-111L7722) for financial support. Y.P.C. and C.W.C. also thank MOST of Taiwan (contract no. MOST 110-2119-M-002-015-MBK) and the Center of Atomic Initiative for New Materials, National Taiwan University, from the Featured Areas Research Center Program within the framework of the Higher Education Sprout Project by the Ministry of Education in Taiwan (111L900802) for financial support.

REFERENCES

- (1) Cao, W.; Kang, J.; Sarkar, D.; Liu, W.; Banerjee, K. 2D Semiconductor FETs—Projections and Design for Sub-10 nm VLSI. *IEEE Trans. Electron Devices* **2015**, *62*, 3459–3469.
- (2) Xu, K.; Chen, D.; Yang, F.; Wang, Z.; Yin, L.; Wang, F.; Cheng, R.; Liu, K.; Xiong, J.; Liu, Q.; et al. Sub-10 nm Nanopattern Architecture for 2D Material Field-Effect Transistors. *Nano Lett.* **2017**, *17*, 1065–1070.
- (3) Liu, H.; Neal, A. T.; Ye, P. D. Channel Length Scaling of MoS₂MOSFETs. *ACS Nano* **2012**, *6*, 8563–8569.
- (4) Zheng, Y.; Gao, J.; Han, C.; Chen, W. Ohmic Contact Engineering for Two-Dimensional Materials. *Cell Rep.* **2021**, *2*, 100298.
- (5) Somvanshi, D.; Kallatt, S.; Venkatesh, C.; Nair, S.; Gupta, G.; Anthony, J. K.; Karmakar, D.; Majumdar, K. Nature of Carrier Injection in Metal/2D-Semiconductor Interface and Its Implications for the Limits of Contact Resistance. *Phys. Rev. B* **2017**, *96*, 205423.
- (6) Sotthewes, K.; van Bremen, R.; Dollekamp, E.; Boulogne, T.; Nowakowski, K.; Kas, D.; Zandvliet, H. J. W.; Bampoulis, P. Universal Fermi-Level Pinning in Transition-Metal Dichalcogenides. *J. Phys. Chem. C* **2019**, *123*, 5411–5420.
- (7) Liu, X.; Choi, M. S.; Hwang, E.; Yoo, W. J.; Sun, J. Fermi Level Pinning Dependent 2D Semiconductor Devices: Challenges and Prospects. *Adv. Mater.* **2022**, *34*, 2108425.
- (8) Kim, C.; Moon, I.; Lee, D.; Choi, M. S.; Ahmed, F.; Nam, S.; Cho, Y.; Shin, H.-J.; Park, S.; Yoo, W. J. Fermi Level Pinning at

Electrical Metal Contacts of Monolayer Molybdenum Dichalcogenides. *ACS Nano* **2017**, *11*, 1588–1596.

(9) Kiriya, D.; Tosun, M.; Zhao, P.; Kang, J. S.; Javey, A. Air-Stable Surface Charge Transfer Doping of MoS₂ by Benzyl Viologen. *J. Am. Chem. Soc.* **2014**, *136*, 7853–7856.

(10) Renau, A. Recent Developments in Ion Implantation. *ECS Trans* **2011**, *35*, 173.

(11) Xu, K.; Zhao, Y.; Lin, Z.; Long, Y.; Wang, Y.; Chan, M.; Chai, Y. Doping of Two-Dimensional MoS₂ by High Energy Ion Implantation. *Semicond. Sci. Technol.* **2017**, *32*, 124002.

(12) Murray, R.; Haynes, K.; Zhao, X.; Perry, S.; Hatem, C.; Jones, K. The Effect of Low Energy Ion Implantation on MoS₂. *ECS J. Solid State Sci. Technol.* **2016**, *5*, Q3050.

(13) Nipane, A.; Karmakar, D.; Kaushik, N.; Karande, S.; Lodha, S. Few-Layer MoS₂ p-Type Devices Enabled by Selective Doping Using Low Energy Phosphorus Implantation. *ACS Nano* **2016**, *10*, 2128–2137.

(14) Loh, L.; Zhang, Z.; Bosman, M.; Eda, G. Substitutional Doping in 2D Transition Metal Dichalcogenides. *Nano Res.* **2021**, *14*, 1668–1681.

(15) Li, M.; Yao, J.; Wu, X.; Zhang, S.; Xing, B.; Niu, X.; Yan, X.; Yu, Y.; Liu, Y.; Wang, Y. P-Type Doping in Large-Area Monolayer MoS₂ by Chemical Vapor Deposition. *ACS Appl. Mater. Interfaces* **2020**, *12*, 6276–6282.

(16) Chuang, H.-J.; Chamlagain, B.; Koehler, M.; Perera, M. M.; Yan, J.; Mandrus, D.; Tomanek, D.; Zhou, Z. Low-Resistance 2D/2D Ohmic Contacts: A Universal Approach to High-Performance WSe₂, MoS₂, and MoSe₂ Transistors. *Nano Lett.* **2016**, *16*, 1896–1902.

(17) Jang, J.; Ra, H.; Ahn, J.; Kim, T. W.; Song, S. H.; Park, S.; Taniguchi, T.; Watanabe, K.; Lee, K.; Hwang, D. K. Fermi-Level Pinning-Free WSe₂ Transistors via 2D Van Der Waals Metal Contacts and Their Circuits. *Adv. Mater.* **2022**, *34*, 2109899.

(18) Suryavanshi, S. V.; Magyari-Kope, B.; Lim, P.; McClellan, C.; Smithe, K. K. H.; English, C. D.; Pop, E. Improving Electric Contacts to Two-Dimensional Semiconductors. *arXiv (Condensed Matter.Mesoscale and Nanoscale Physics)*, May 22, 2021, 2105.10792, ver. 1. DOI: 10.48550/arXiv.2105.10792

(19) Yang, L.; Majumdar, K.; Liu, H.; Du, Y.; Wu, H.; Hatzistergos, M.; Hung, P. Y.; Tieckelmann, R.; Tsai, W.; Hobbs, C.; et al. Chloride Molecular Doping Technique on 2D Materials: WS₂ and MoS₂. *Nano Lett.* **2014**, *14*, 6275–6280.

(20) Fang, H.; Tosun, M.; Seol, G.; Chang, T. C.; Takei, K.; Guo, J.; Javey, A. Degenerate N-Doping of Few-Layer Transition Metal Dichalcogenides by Potassium. *Nano Lett.* **2013**, *13*, 1991–1995.

(21) Liu, X.; Qu, D.; Ryu, J.; Ahmed, F.; Yang, Z.; Lee, D.; Yoo, W. J. P-type Polar Transition of Chemically Doped Multilayer MoS₂ Transistor. *Adv. Mater.* **2016**, *28*, 2345–2351.

(22) Ji, H. G.; Solis-Fernández, P.; Yoshimura, D.; Maruyama, M.; Endo, T.; Miyata, Y.; Okada, S.; Ago, H. Chemically Tuned P-and N-Type WSe₂ Monolayers with High Carrier Mobility for Advanced Electronics. *Adv. Mater.* **2019**, *31*, 1903613.

(23) Kwon, S.-J.; Han, T.-H.; Ko, T. Y.; Li, N.; Kim, Y.; Kim, D. J.; Bae, S.-H.; Yang, Y.; Hong, B. H.; Kim, K. S.; et al. Extremely Stable Graphene Electrodes Doped with Macromolecular Acid. *Nat. Commun.* **2018**, *9*, 2037.

(24) Lin, J. D.; Han, C.; Wang, F.; Wang, R.; Xiang, D.; Qin, S.; Zhang, X.-A.; Wang, L.; Zhang, H.; Wee, A. T. S.; et al. Electron-Doping-Enhanced Trion Formation in Monolayer Molybdenum Disulfide Functionalized with Cesium Carbonate. *ACS Nano* **2014**, *8*, 5323–5329.

(25) Ho, P.-H.; Yeh, Y.-C.; Wang, D.-Y.; Li, S.-S.; Chen, H.-A.; Chung, Y.-H.; Lin, C.-C.; Wang, W.-H.; Chen, C.-W. Self-Encapsulated Doping of n-Type Graphene Transistors with Extended Air Stability. *ACS Nano* **2012**, *6*, 6215–6221.

(26) Rai, A.; Valsaraj, A.; Movva, H. C. P.; Roy, A.; Ghosh, R.; Sonde, S.; Kang, S.; Chang, J.; Trivedi, T.; Dey, R.; et al. Air Stable Doping and Intrinsic Mobility Enhancement in Monolayer Molybdenum Disulfide by Amorphous Titanium Suboxide Encapsulation. *Nano Lett.* **2015**, *15*, 4329–4336.

- (27) McClellan, C. J.; Yalon, E.; Smithe, K. K. H.; Suryavanshi, S. v.; Pop, E. High Current Density in Monolayer MoS₂ Doped by AlO_x. *ACS Nano* **2021**, *15*, 1587–1596.
- (28) Yamamoto, M.; Nakaharai, S.; Ueno, K.; Tsukagoshi, K. Self-Limiting Oxides on WSe₂ as Controlled Surface Acceptors and Low-Resistance Hole Contacts. *Nano Lett.* **2016**, *16*, 2720–2727.
- (29) Zhao, P.; Kiriya, D.; Azcatl, A.; Zhang, C.; Tosun, M.; Liu, Y.-S.; Hettick, M.; Kang, J. S.; McDonnell, S.; KC, S.; et al. Air Stable P-Doping of WSe₂ by Covalent Functionalization. *ACS Nano* **2014**, *8*, 10808–10814.
- (30) Zhang, F.; Lu, Y.; Schulman, D. S.; Zhang, T.; Fujisawa, K.; Lin, Z.; Lei, Y.; Elias, A. L.; Das, S.; Sinnott, S. B.; et al. Carbon Doping of WS₂ Monolayers: Bandgap Reduction and p-Type Doping Transport. *Sci. Adv.* **2019**, *5*, No. eaav5003.
- (31) Tang, B.; Yu, Z. G.; Huang, L.; Chai, J.; Wong, S. L.; Deng, J.; Yang, W.; Gong, H.; Wang, S.; Ang, K.-W.; et al. Direct N-to p-Type Channel Conversion in Monolayer/Few-Layer WS₂ Field-Effect Transistors by Atomic Nitrogen Treatment. *ACS Nano* **2018**, *12*, 2506–2513.
- (32) Chee, S.-S.; Jang, H.; Lee, K.; Ham, M.-H. Substitutional Fluorine Doping of Large-Area Molybdenum Disulfide Monolayer Films for Flexible Inverter Device Arrays. *ACS Appl. Mater. Interfaces* **2020**, *12*, 31804–31809.
- (33) Raita, M.; Denchokepragay, N.; Champreda, V.; Laosiripojana, N. Effects of Alkaline Catalysts on Acetone-Based Organosolv Pretreatment of Rice Straw. *3 Biotech* **2017**, *7*, 340.
- (34) Tichit, D.; Naciri Bennani, M.; Figueras, F.; Tessier, R.; Kervennal, J. Aldol Condensation of Acetone over Layered Double Hydroxides of the Meixnerite Type. *Appl. Clay Sci.* **1998**, *13*, 401–415.
- (35) Mak, K. F.; He, K.; Lee, C.; Lee, G. H.; Hone, J.; Heinz, T. F.; Shan, J. Tightly Bound Trions in Monolayer MoS₂. *Nat. Mater.* **2013**, *12*, 207–211.
- (36) Chakraborty, B.; Bera, A.; Muthu, D. V. S.; Bhowmick, S.; Waghmare, U. v.; Sood, A. K. Symmetry-Dependent Phonon Renormalization in Monolayer MoS₂ Transistor. *Phys. Rev. B* **2012**, *85*, 161403.
- (37) Addou, R.; Colombo, L.; Wallace, R. M. Surface Defects on Natural MoS₂. *ACS Appl. Mater. Interfaces* **2015**, *7*, 11921–11929.
- (38) Pető, J.; Ollár, T.; Vancsó, P.; Popov, Z. I.; Magda, G. Z.; Dobrik, G.; Hwang, C.; Sorokin, P. B.; Tapasztó, L. Spontaneous Doping of the Basal Plane of MoS₂ Single Layers through Oxygen Substitution under Ambient Conditions. *Nat. Chem.* **2018**, *10* (12), 1246–1251.
- (39) Vancsó, P.; Magda, G. Z.; Pető, J.; Noh, J.-Y.; Kim, Y.-S.; Hwang, C.; Biró, L. P.; Tapasztó, L. The Intrinsic Defect Structure of Exfoliated MoS₂ Single Layers Revealed by Scanning Tunneling Microscopy. *Sci. Rep.* **2016**, *6*, 29726.
- (40) Lee, D.; Lee, J. J.; Kim, Y. S.; Kim, Y. H.; Kim, J. C.; Huh, W.; Lee, J.; Park, S.; Jeong, H. Y.; Kim, Y. D.; Lee, C.-H. Remote Modulation Doping in van Der Waals Heterostructure Transistors. *Nat. Electron.* **2021**, *4*, 664–670.
- (41) Allain, A.; Kang, J.; Banerjee, K.; Kis, A. Electrical Contacts to Two-Dimensional Semiconductors. *Nat. Mater.* **2015**, *14*, 1195–1205.
- (42) Ber, E.; Grady, R. W.; Pop, E.; Yalon, E. Pinpointing the Dominant Component of Contact Resistance to Atomically Thin Semiconductors. *arXiv (Physics Applied Physics)*, October 6, 2021, 2110.02563, ver. 1. DOI: 10.48550/arXiv.2110.02563
- (43) Chen, S.-Y.; Ho, P.-H.; Shiue, R.-J.; Chen, C.-W.; Wang, W.-H. Transport/Magnetotransport of High-Performance Graphene Transistors on Organic Molecule-Functionalized Substrates. *Nano Lett.* **2012**, *12*, 964–969.
- (44) Chang, M.-C.; Ho, P.-H.; Tseng, M.-F.; Lin, F.-Y.; Hou, C.-H.; Lin, I.; Wang, H.; Huang, P.-P.; Chiang, C.-H.; Yang, Y.-C.; et al. Fast Growth of Large-Grain and Continuous MoS₂ Films through a Self-Capping Vapor-Liquid-Solid Method. *Nat. Commun.* **2020**, *11*, 3682.

Recommended by ACS

Precision Modification of Monolayer Transition Metal Dichalcogenides via Environmental E-Beam Patterning

Ryan Selhorst, Rahul Rao, *et al.*

JANUARY 23, 2023
ACS NANO

READ 

Hydrogen-Doping-Enabled Boosting of the Carrier Mobility and Stability in Amorphous IGZO Transistors

Jeonga Lee, Jae Kyeong Jeong, *et al.*

DECEMBER 13, 2022
ACS APPLIED MATERIALS & INTERFACES

READ 

In Situ Synthesis of Two-Dimensional Lateral Semiconducting-Mo:Se//Metallic-Mo Junctions Using Controlled Diffusion of Se for High-Performance Large-S...

Arindam Bala, Sunkook Kim, *et al.*

JANUARY 06, 2023
ACS NANO

READ 

In-Memory Tactile Sensor with Tunable Steep-Slope Region for Low-Artifact and Real-Time Perception of Mechanical Signals

Shisheng Chen, Benhui Hu, *et al.*

JANUARY 23, 2023
ACS NANO

READ 

Get More Suggestions >